



Fatigue fracture morphology of AISI H13 steel obtained by additive manufacturing

Wojciech Macek · Rui F. Martins · Ricardo Branco · Zbigniew Marciniak · Mirosław Szala · Sebastian Wroński

Received: 18 October 2021 / Accepted: 10 December 2021
© The Author(s) 2022

Abstract The paper focuses on researching the effect of fatigue loading on metallic structure, lifetime, and fracture surface topographies in AISI H13 steel specimens obtained by selective laser melting (SLM). The topography of the fracture surfaces was measured over their entire area, according to the entire total area method, with an optical three-dimensional surface measurement system. The fatigue results of the SLM 3D printed steel specimens were compared with those reported for conventionally manufactured 13H steel. The investigation also considers the roughness of the specimens' side surface. Moreover, the fractographic

evaluation conducted using scanning electron microscopy confirms that the predominant fracture mechanism is transgranular fracture. Microtomography done after mechanical loading also showed the influence of the stress level on the porosity distribution. Both fractographic and Micro-CT investigations confirm that higher stresses result in coarser and much more uniform porosity observed in fractured samples. These comprehensive quantitative and qualitative fracture analyses are beneficial to predict the failure conditions of SLM steel parts, especially in the case of fatigue damage. From the quantitative analysis of the H13

W. Macek (✉)
Faculty of Mechanical Engineering and Ship Technology,
Gdańsk University of Technology, Gabriela Narutowicza
11/12, 80-233 Gdańsk, Poland
e-mail: wojciech.macek@yahoo.com

W. Macek
Advanced Materials Center, Gdańsk University of
Technology, ul. Narutowicza 11/12, 80-233 Gdańsk,
Poland

R. F. Martins
UNIDEMI, Department of Mechanical and Industrial
Engineering, Nova School of Science and Technology,
Universidade NOVA de Lisboa, Campus de Caparica,
2829-516 Caparica, Portugal

R. Branco
CEMMPRE, Department of Mechanical Engineering,
University of Coimbra, Rua Luís Reis Santos, Pinhal de
Marrocos, 3030-788 Coimbra, Portugal

Z. Marciniak
Faculty of Mechanical Engineering, Opole University of
Technology, Mikołajczyka 5, 45-271 Opole, Poland

M. Szala
Department of Materials Engineering, Faculty of
Mechanical Engineering, Lublin University of
Technology, Nadbystrzycka 36D, 20-816 Lublin, Poland

S. Wroński
Faculty of Physics and Applied Computer Science, AGH
University of Science and Technology, al.Mickiewicza
30, 30-059 Kraków, Poland

SLM-manufactured fracture surface topography, it was possible to conclude that the larger the loadings acting on the specimen, the rougher the fracture surface because the ductile fracture mode dominates. It has also been proven that the porosity degree changes along the length of the sample for the most stressed specimens.

Keywords H13 steel · Selective laser melting (SLM) · Mechanical properties · Surface metrology · Fractography · Micro-CT

Abbreviations

D_f	Fractal dimension (–)
σ_{\max}	Maximum stress (MPa)
N_f	Number of cycles to failure (cycles)
R	Load ratio (–)
Rq	Root-mean-square (RMS) deviation of the roughness profile (μm)
Ra	Arithmetic mean deviation of the roughness profile (μm)
Rv	Maximum valley depth of the roughness profile (μm)
Sk	Core roughness depth (mm)
Spk	Reduced peak height (μm)
Svk	Reduced valley depth (μm)
Sq	Root average square height (mm)
Vv	Void volume (mm^3/mm^2)

1 Introduction

Since the 1990s (Beaman and Deckard 1989), additive manufacturing (AM) technologies have been intensely expanded, proper to their versatility as efficient techniques for metal processing (Beaman and Deckard 1989; Carneiro et al. 2019; Jesus et al. 2021). The selective laser melting (SLM) manufacturing process is fast-growing and extensively used for the fabrication of complex elements in the aerospace, medical, and mould industries (Razavi and Berto 2018; Santos et al. 2016). The AISI H13 grade is conventionally dedicated for metal tools subjected to high operation at elevated temperatures. This type of steel has excellent resistance to thermal fatigue, erosion, and sliding wear (Walczak and Szala 2021), and currently, the H13-grade metallic powder is employed to produce moulds and dies using

SLM (Fonseca et al. 2020; Xue et al. 2013). However, the mechanical features of the parts obtained by the metallic powder bed fusion strongly depend on the manufacturing parameters (Kurzynowski et al. 2012), and manufacturing orientations, as concluded by Nagahama et al. (2019) through uniaxial tensile tests.

Investigations into fracture mechanisms are pivotal, particularly for additively manufactured components, because they are highly susceptible to a number of defects, namely micro-cracks and porosities, which may result in material lack of coherence (Romano et al. 2020; Wang et al. 2019). Therefore, various methods have been employed to study the crack propagation during the material fatigue process and the fatigue damage failure analysis. Numerous mechanisms of crack nucleation and propagation have been described in additive manufacturing materials. For example, dimples and cleavage of the tensile fracture surface were analysed by Weng et al. (2020). They found that the tensile fracture surface of the as-built IN100 was dominated by dimples, corresponding to the higher elongation rate. In contrast, Khosravani et al. (2020) presented a reviewed fracture behaviour of 3D-printed polymeric and metallic parts, which have been examined under various experimental campaigns. The authors pointed out that the fracture behaviour and failure modes of 3D-printed components is essential to ensure safe mechanical stresses during their service life.

The material's morphology can be examined within the material (Wang et al. 2019; Hebda et al. 2020; Fisher and Marquis 2016) and on its surface (Macek et al. 2020d; Kida et al. 2017; Lauschmann and Šiška 2012). Scanning electron microscopy (SEM) is most often used to obtain data about the fracture mechanism, such as non-metallic inclusions (Kowal and Szala 2020) or other imperfections in materials (Moussa et al. 2021). Three-dimensional surface profilometry has also been used to study the tribological response of SiC fracture surfaces (Huang and Feng 2006) and to develop a dynamic friction model sensitive to overstress and relaxation phenomena. Post-failure techniques measuring fracture surface parameters after standard fatigue tests can be important tools for lifetime estimation and must be experimentally validated (Cisko et al. 2019). There are several successfully studies in which scientists have tried to combine all possible methods and link the surface parameters to fracture mechanisms or fatigue life, especially using surface roughness

accounted for in the entire area of the fracture surfaces (Pomberger et al. 2020; Slámečka et al. 2010; Sampath et al. 2018; Macek et al. 2020a). Summing up, the literature provides studies that usually focus on one of the listed above aspects relating to fracture analysis. On the other hand, the comprehensive fracture investigation is useful for identifying the load history, which is further essential to identify the failure cause. Therefore, this work develops the research method for fracture surface topography analysis proposed in previous papers (Macek 2019a, b; Macek et al. 2020b, c) and links it with the fatigue testing conditions based on a fractography analysis. In the current paper, the surface analysis was performed on the entire fracture area without dividing the observation area into subregions. Moreover, the failure conditions associated with the different load histories are discussed on the basis of fracture analysis. The work also aims to indicate the characteristic features of the fatigue fractures of the SLM specimens by relating them to the loading conditions and the fractographic evaluation.

Following the Introduction, the paper is organised as follows: Sect. 2 describes the materials and methods used for this research. Section 3 gathers information on the experimental fatigue and fracture surface programs. Section 4 presents the primary outcomes of the fatigue campaign and the fracture surface parameters. The paper ends with a summary of the most relevant findings.

2 Materials and methods

2.1 Material preparation for fatigue uniaxial testing

The H13 steel specimens were manufactured with the usage of a SLM Solutions SLM 125 industrial 3D printer and commercial powder. SLM additive process parameters used in the fabrication of the tested specimens are given according to our previous study (Garcias et al. 2021), with energy densities ranging from 92.59 to 111.11 J/mm³, and laser speeds of 300 and 250 mm/s, respectively. The metallic powder used in the specimens had dimensions between 10 and 45 µm, whose chemical composition is described in Table 1. The specimens for fatigue testing were printed in the vertical direction, according to the geometry exhibited in Fig. 1, and were not subjected to any heat

treatment. All specimens were additively manufactured using the same parameters. After the manufacturing process, the surface was machined and polished mechanically using progressively finer sandpapers (P300, P500, P1000, P1500, P2000, and P2500) followed by 6-µm diamond paste compound. The final average roughness was $R_a = 0.172$ µm. Then, the specimens were tested with different fatigue loading parameters. The results were compared with those of the H13 conventionally manufactured steel (see Fig. 4) which was supplied in the form of 20 mm thick plates. The steel was annealed at 650 °C for 2 h and then slowly cooled in furnace. The specimens were machined in a CNC turning centre and then the surfaces were polished as described for the SLM samples.

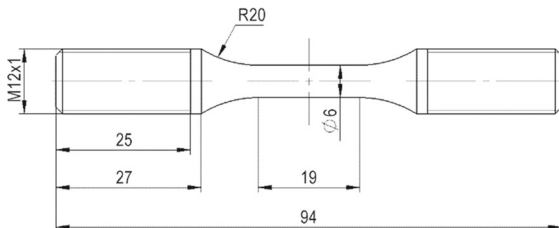
The H13 specimens produced by SLM were tested using an Instron 8802 fatigue machine, with a maximum load cell of 100 kN, under uniaxial conditions (see Fig. 2). The tests were performed at a load ratio $R = 0.2$ with a frequency of 1 Hz for the highest load values, 2 Hz for the intermediate load levels, and 5 Hz for the load level at which it was expected to reach infinite life. All tests were carried out at room temperature. Two specimens were used for each load level, for at least four different stress levels in the finite life region. Test pieces that reached two million cycles were considered infinite life (run out). The nominal stress levels are presented, inter alia, in Table 2, together with the results of surface topography measurements.

2.2 Analysis of fracture and microstructure behavior

Topographic measurements of the fracture surfaces were performed with an Alicona G4 optical profilometer using focus-variation technology with a $\times 10$ lens (see Fig. 3a). Due to the restricted field of view, eight rows and seven columns were stitched together to map the entire fracture surface area. The fracture surface maps were processed with MountainsMap® software for quantitative analysis and visualisation. A similar configuration of equipment and software for surface analysis was used in the works (Allum et al. 2020; Kahlin et al. 2020). Additionally, the fractures of the fatigue specimens were also observed under specific magnification using a Phenom desktop Scanning Electron Microscope (SEM) as described elsewhere (Żebrowski et al. 2019) (see Fig. 3b).

Table 1 Chemical composition (wt.%) of the metallic powder used in the production of the SLM specimens

	Fe	C	Cr	Mn	Mo	Ni + Cu	P	S	Si	V
AISI H13 (10–45 μm)	Bal	0.32–0.45	4.75–5.50	0.20–0.60	1.10–1.75	0.75	0.03	0.03	0.80–1.25	0.8–1.20

**Fig. 1** Specimen geometry used in the fatigue campaign (units: mm)**Fig. 2** Servo-hydraulic machine used to carry out the fatigue tests

The microtomography measurements presented in this paper were performed using a Nanotom 180 N device (see Fig. 3c) produced by GE Sensing & Inspection Technologies phoenix X-ray GmbH. The machine is equipped with nanofocus X-ray tube with maximum 180 kV voltage. The tomograms were registered on Hamamatsu 2300 2300 pixel detector. The reconstruction of measured objects was done with the aid of proprietary GE software datosX ver. 2.1.0 with use of Feldkamp algorithm for cone beam X-ray CT (Feldkamp et al. 1984). The post reconstruction

data treatment was performed using VGStudio Max 2.1 (Volume Graphics GmbH 2013) and free Fiji software (<http://fiji.sc/Fiji>). All examined specimens were scanned at 160 kV of source voltage and 140 μA , with a rotation of the specimen of 360° in 2800 steps. To reduce the beam hardening effect, the copper filter (thickness 500 μm) was used. The exposure time was 500 ms and a frame averaging of 3 images was applied. The reconstructed images had a voxel size of (5.0 μm) (Jesus et al. 2021).

The scanned data were analysed qualitatively and quantitatively. The 3D data was saved as a series of images (image stack) representing the successive cross-sections of each sample. For each image (sections), the porosity evaluated after mechanical loading, was determined and the mean pore size (with standard deviation) was calculated. It is worth noting that the analysis performed in this way gives information about the pore size only in the transverse plane of the sample. In order to perform the calculations, the BoneJ plug and the Thickness function from Fiji/ImageJ were used.

3 Results

Fatigue results in form of S–N curves for both the additively manufactured and conventional specimens are shown in Fig. 4. Overall, the maximum applied stress can be successfully related to the number of cycles to failure via power functions. As can be seen, the fitted curves present high correlation coefficients. In the case of the SLM samples, the scatter is higher, which can be explained by the specificities of the manufacturing process which is more susceptible to defects. Besides, the details about the fatigue loads and fatigue lives as well as the fracture surface topography measurements are presented in Table 2. The maximum and minimum values of individual fracture surface parameters are marked in green and yellow,

Table 2 Summary of the fatigue testing program and fracture surface measurements for AISI H13 by SLM

Parameter	Specimen														
	B2a ^a	B2b ^b	B3b	B4a	B4b	B5a	B5b	B8a	B8b	C5a	C5b	C6a	C6b		
Sq	mm	Root-mean-square height	0.19	0.18	<i>0.35</i>	0.17	0.19	0.22	0.23	0.26	0.24	0.13	0.16	0.07	0.08
Vv	mm ³ / mm ²	Void volume	0.24	0.27	<i>0.46</i>	0.23	0.24	0.27	0.33	0.32	0.31	0.17	0.21	0.10	0.09
Sk	mm	Core roughness depth	0.46	0.39	<i>1.02</i>	0.34	0.42	0.46	0.46	0.62	0.68	0.36	0.42	0.17	0.19
Df	–	Fractal dimension	2.21	2.21	2.14	2.19	2.18	2.19	2.18	2.20	2.19	2.19	2.18	2.29	2.24
Rq	μm	Root-mean-square (RMS) deviation of the roughness profile	0.55		<i>0.78</i>	0.73		0.51		0.70		0.83		<i>0.88</i>	
Ra	μm	Arithmetic mean deviation of the roughness profile	0.43		<i>0.48</i>	0.56		0.39		0.49		0.55		<i>0.64</i>	
Rv	μm	Maximum valley depth of the roughness profile	2.05		<i>4.79</i>	2.70		1.76		3.02		<i>6.45</i>		3.06	
σ _{max}	MPa	Maximum stress	200		<i>300</i>	100		100		200		90		90	
σ _m	MPa	Mean stress	120		<i>180</i>	60		60		120		54		54	
σ _{min}	MPa	Minimum stress	40		<i>60</i>	20		20		40		18		18	
N _f	cycle	Number of cycles to failure	6282		580	132,544		412,216		39,601		<i>461,964</i>		41,638	

Italics: maximum values of individual parameters; bold: minimum values of individual parameters

^aa—longer part of the broken the specimen

^bb—shorter part of the broken the specimen

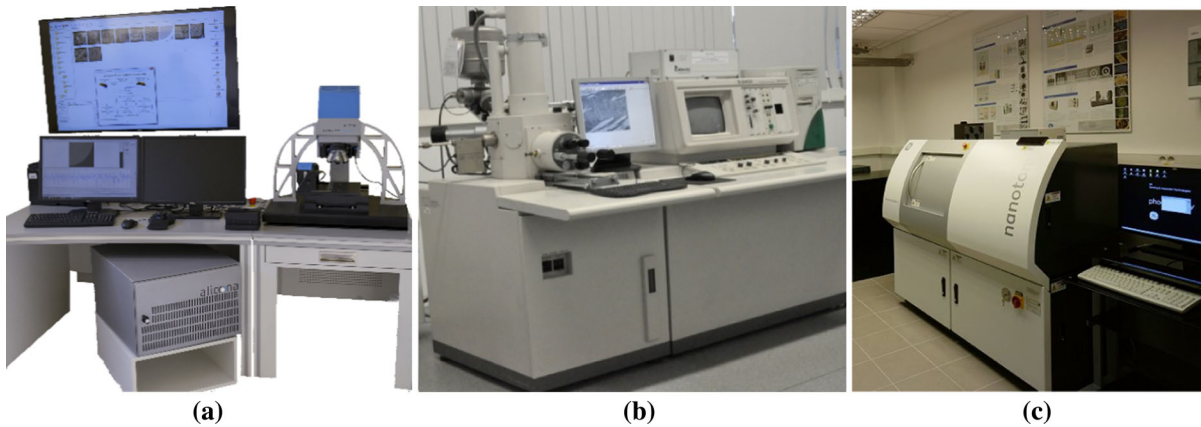


Fig. 3 **a** Infinite focus IF G4 measurement device used in surface metrology, **b** phenom desktop scanning electron microscope (SEM), **c** micro-CT scanner Nanotom 180N

respectively. The selected parameters in Table 2 have been divided into three types (Fig. 5):

- entire fracture primary surface parameters: Sq, Vv, Sk, Df (see Fig. 6);
- side surface profile of the specimen, measured before fatigue test: Rq, Ra, Rv (see Fig. 7);
- fatigue test parameters and results: σ_{max}, N_f (see Fig. 4).

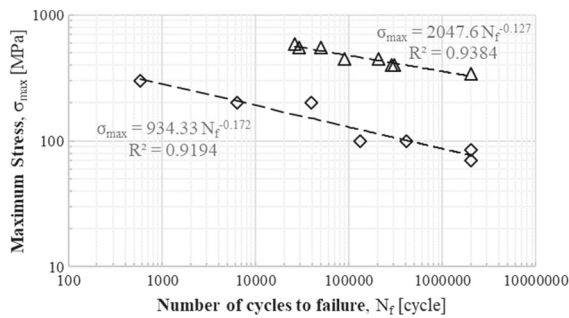


Fig. 4 SN diagrams (σ_{\max} vs. N_f) for AISI H13 by SLM (diamonds) and conventional manufacture (triangles). Load ratio, $R = 0.2$. Fatigue results of the conventional manufactured specimens were taken from the reference Garcias et al. (2021)

The side surface profile of the specimen R-parameters does not correlate with the load values, which results from the large irregularity of the valley distribution on the specimen surface and the randomness of the applied measurement profile. Therefore, the profile results, measured as in Fig. 7, will not be used for further analyses. The surface parameters of fatigue fractures, as shown in Fig. 6, will be analysed further, especially in combination with the loads.

As shown in Fig. 5, there are specific dissidences between the different fracture zones. In Fig. 5 are also shown the depth histograms related to the analyzed example fracture surface. The depth histogram represents the distribution density of the surface data points. The horizontal axis is depicted in percent of the total number and the vertical one in depths, followed by the Abbott-Firestone (Abbott and Firestone 1933; Deepak Lawrence et al. 2014) curve shown in red. Also, the Furrows plot displays all furrows and results for maximum furrow depth, mean furrow depth, and furrows' mean density. The contour lines reveal that in all areas of the fracture, the peaks and valleys form a collection of irregular geometries in different subregions of the measured samples. However, given the promising results, especially for fatigue and fracture investigations, the authors decided to employ the total fracture surface method used by Macek et al. (2021a).

Figure 6 shows fracture surfaces of specimens obtained after fatigue test received with the Infinite-Focus IF G4 variable focal length microscope. The whole current surface was reduced to eliminate the final break, discontinuities, and non-sampling areas. Regions of interest are also presented in isometric views. SLM specimens are denoted with B and C

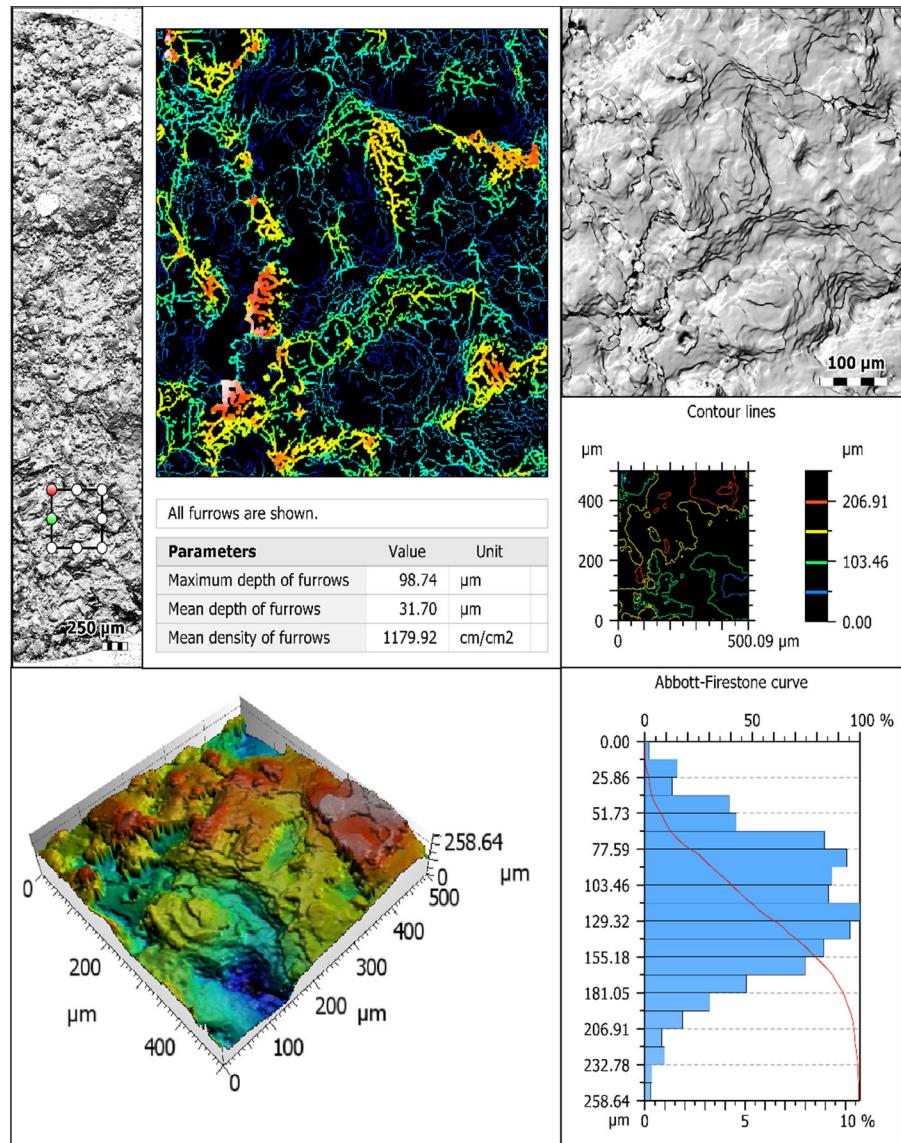
letters, while A15 specimen represents the fracture surface of a conventional manufactured specimen subjected to fatigue loading. The pseudo-color views of the SLM-based specimens are more random than those of the conventional one. In the latter case, the changes are more uniform and progressive along the entire surface. This fact is predictable, because the additively manufactured samples, due to the nature of the fabrication process, contain more defects disperse throughout the fracture surface, which affects the fracture topology.

Figure 8 shows typical three-dimensional visualizations of the tested samples. For each of them, a model was presented using the isosurface function (presenting the surface of the examined object) and a model using the transparence function, which enables visualization of the spatial distribution of pores inside the sample volume. As the data show, the fracture plane for samples B3 and B5 has a much more irregular shape than that of the samples C5 and C6. There is a clear step in sample B3. When we analyze the spatial distribution of pores, it can be seen that it is quite homogeneous for samples B5 and C5. In turn, for samples B3 and C6, it can be seen that porosity after mechanical loading changes along the length of the sample. The variation in porosity shows a certain periodicity.

4 Discussion

To check the fracture surface dependency on the fatigue loading conditions, selected height (S_q) parameters and functional parameters having stratified surface (S_k) and volume (V_v) properties were measured according to the ISO 25178-2 standard (ISO - ISO 2012; Todhunter et al. 2017). Core roughness depth parameter, S_k , showed the highest compliance with the parameters of fatigue tests. The parameters carry out a separation of the height distribution represented by the Abbott curve into three parts: (1) related with the peaks (S_{pk}), (2) the core area (S_k), and (3) for the valleys (S_{vk}) (Țălu et al. 2020; Macek et al. 2021b). A graphical interpretation of the S_k parameters is provided in Fig. 13. On the other hand, a graphical interpretation of the parameters root-mean-square height S_q , void volume V_v and fractal dimension D_f is presented later in the paper, in Figs. 12, 14, 15, respectively.

Fig. 5 Visualization of exemplary fracture area with the furrows, contour lines, and depth histogram



4.1 Fracture surface parameters dependency on fatigue loadings

Figures 9 and 10 show, respectively, the relationship between the fatigue loading and the fracture surface parameters, and the relationship between the fatigue life and the fracture surface parameters for the AISI H13 SLM steel specimens.

The analysis of the fracture surfaces based on the entire fracture surface method using the selected surface topography parameters (see Fig. 9a) confirmed that surface parameters values grow with fatigue loadings for both surface parameters S_q

(Eq. 1) and S_k and volume parameter V_v (Eq. 2). The opposite situation was noted for the fractal dimension D_f (see Fig. 9b). The research results also indicate a strong influence of the maximum stress σ_{\max} in the fracture surface roughness, but most for the results characterized by the parameter core height, S_k . The proportion of the variance for a dependent variable, expressed as R^2 , is approximately 0.68. The fractal dimension D_f is also consistent for the linear approximation, but the proportion of the R^2 is only 0.15. Fatigue test results N_f compared with the analysed fracture surface parameters (see Fig. 10) do not show unequivocal relationships.

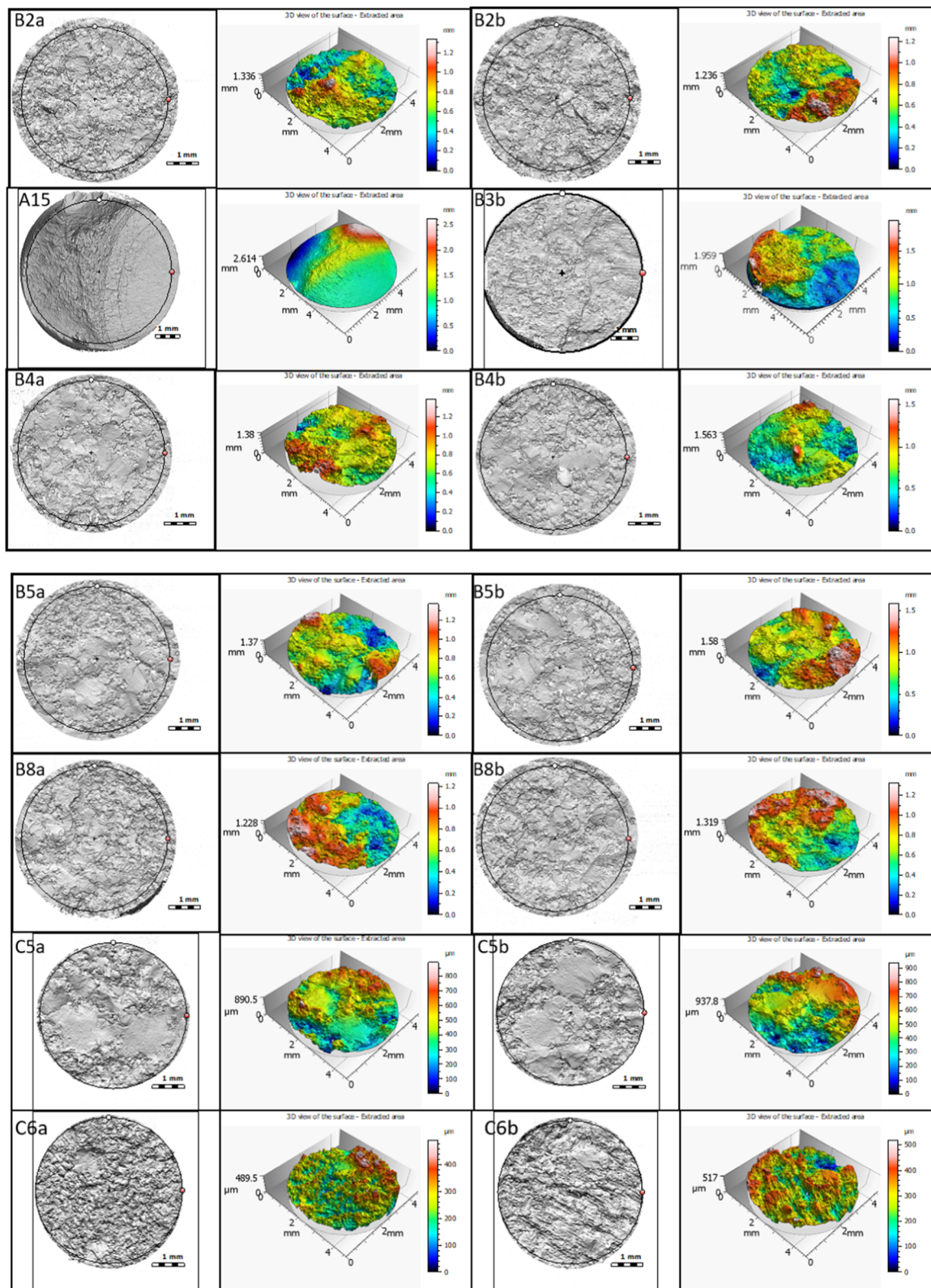


Fig. 6 Fracture surfaces in pseudo-color views

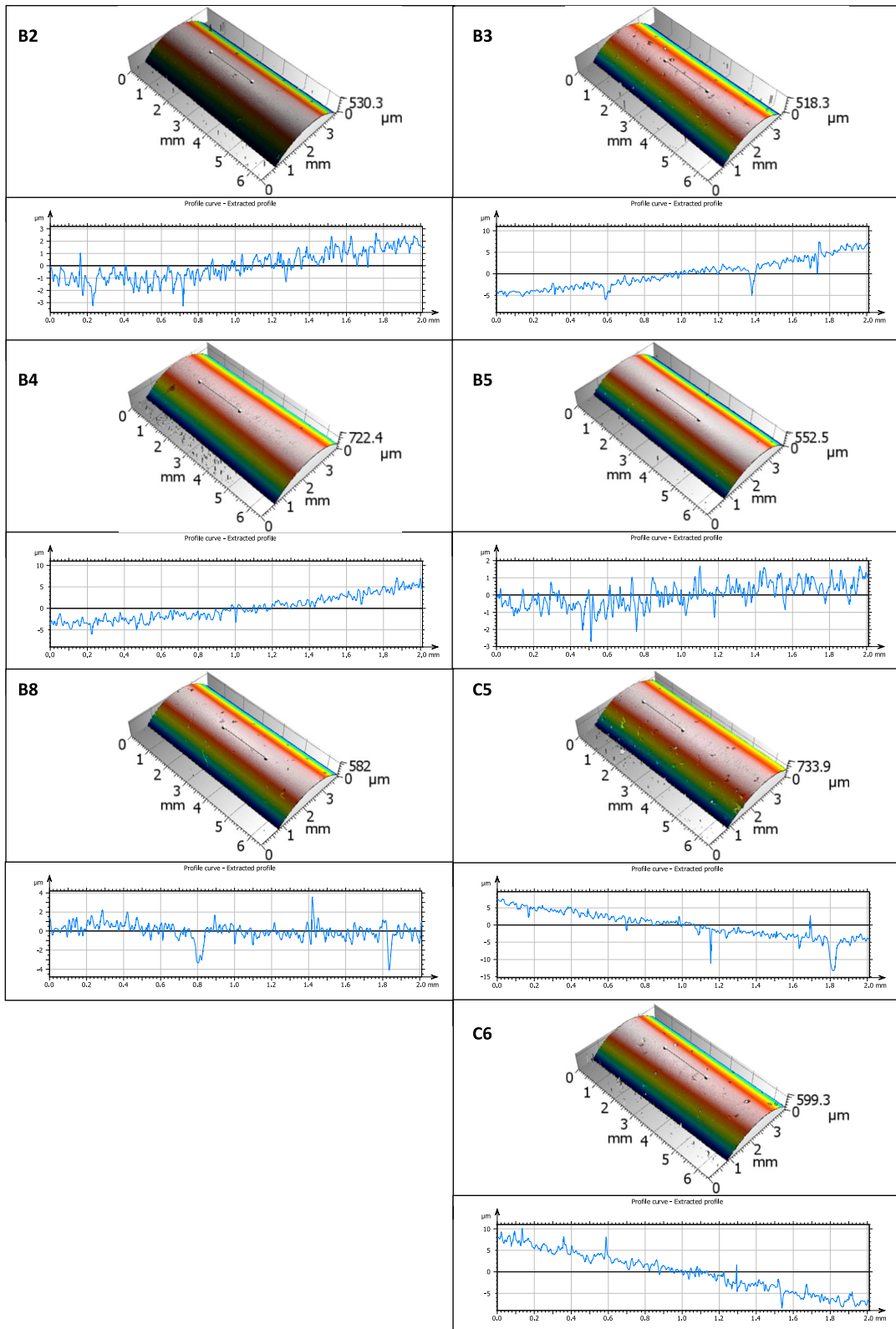


Fig. 7 Side surface profile of the specimen, measured before the fatigue tests

S_q (Eq. 1) is the root mean square height, while void volume V_v calculated for a material ratios S_{mr} , by integrating the volume enclosed above the surface and below a horizontal cutting plane (Eq. 2). Graphical illustration of the functional (volume) parameters is presented in Fig. 11.

$$S_q = \sqrt{\frac{1}{A} \iint_A z^2(x, y) dx dy}, \quad (1)$$

where A is the definition area; z is the surface height in position x, y ; x, y are the lengths in perpendicular directions.

$$V_v(S_{mr}) = k \int_{S_{mr}}^{100\%} [h(S_{mr}) - h(S_{mr}x)] dS_{mr}x, \quad (2)$$

where h is a height; k is a factor to convert the volume into the required unit; for $S_{mr} = 100\%$, the V_v parameter is zero; for $S_{mr} = 0\%$, the void volume is a maximum (the cutting plane below the lowest point); for these cases, the areal material ratio $S_{mr} = S_{mr1} = 10\%$ (see Fig. 11).

The fractal dimension D_f was calculated using the enclosing boxes method (EBM) from the extracted final fracture surface areas. The EBM divides the profile into smaller sections with a width ε and calculates the field A_ε of all fields covering the entire profile. This is an iterative procedure in which the width of the field is changed to plot, $\ln(A_\varepsilon)/\ln(\varepsilon)$.

A comparison was made for the fractal dimension D_f , void volume V_v , core roughness depth S_k and root average square height S_q values (see Fig. 12) of the additively manufactured specimens subjected to fatigue loading. Overall, there is a very good correlation between these variables, and the data can be successfully fitted using linear functions for all cases. V_v shows the highest compliance with S_q ($R^2 = 0.98$), which results from the method of calculating both parameters.

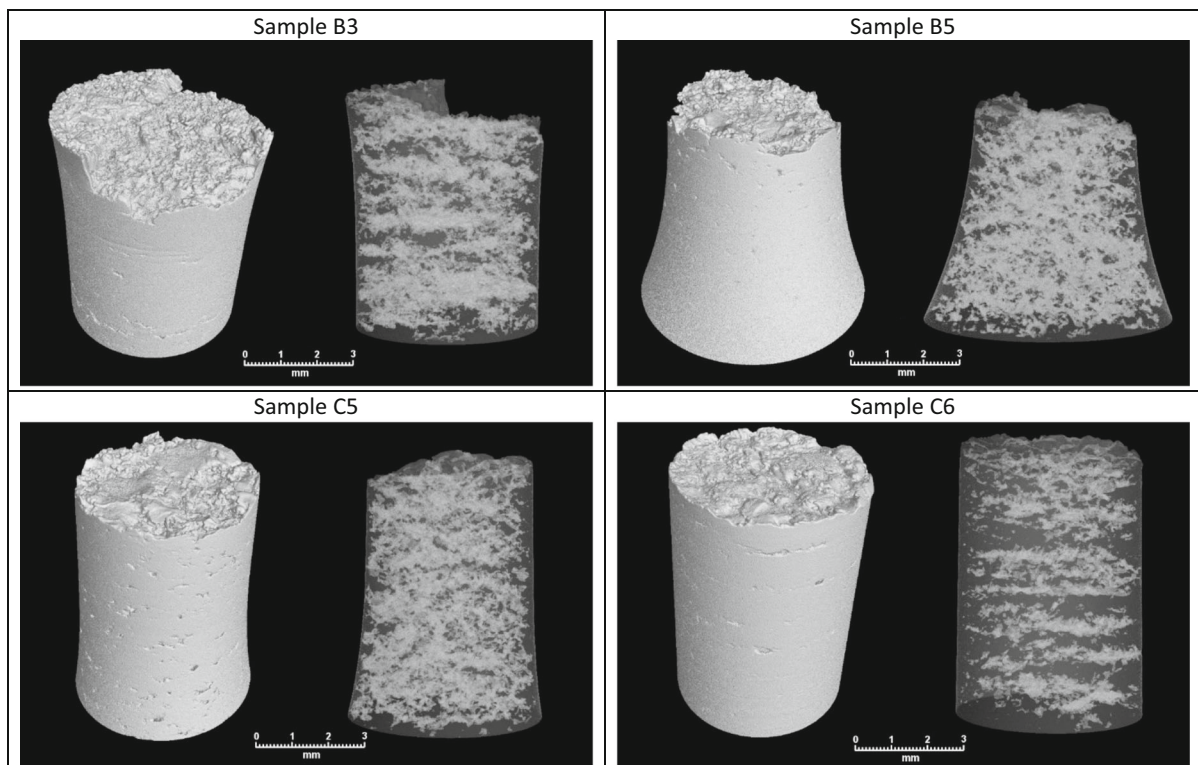
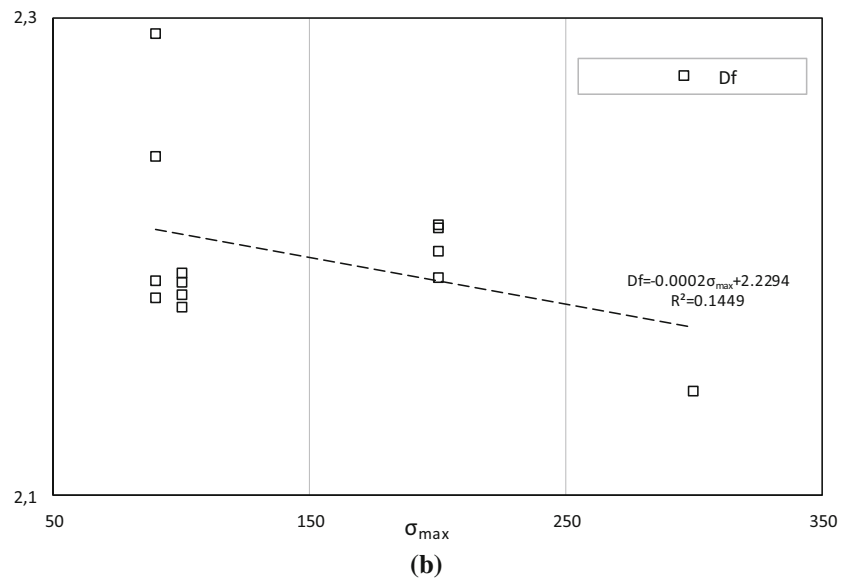
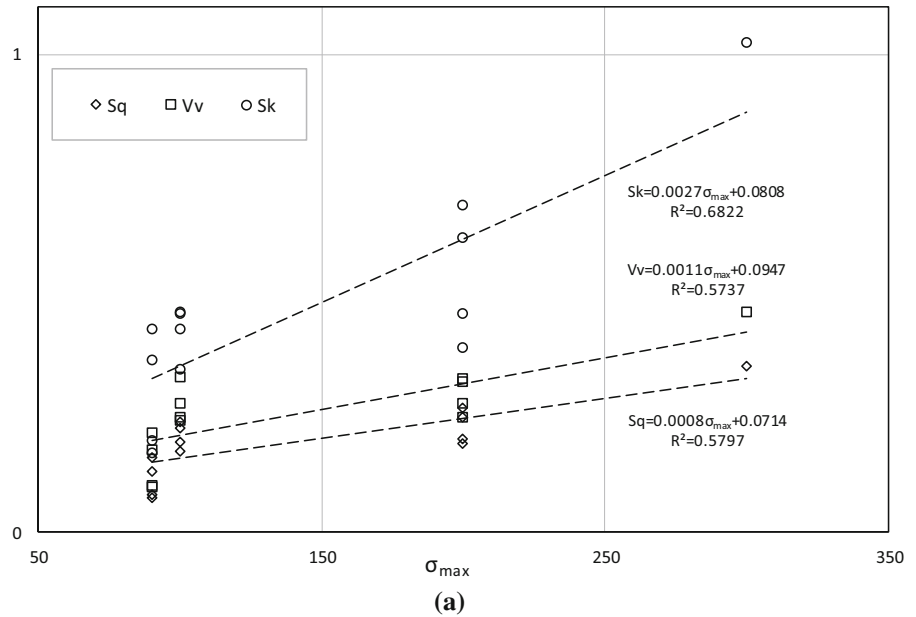


Fig. 8 Three-dimensional micro tomography visualizations of samples B3, B5, C5 and C6

Fig. 9 Maximum stress σ_{max} vs. fracture surface measurement for: **a** Sq, Vv, Sk; and **b** fractal dimension Df



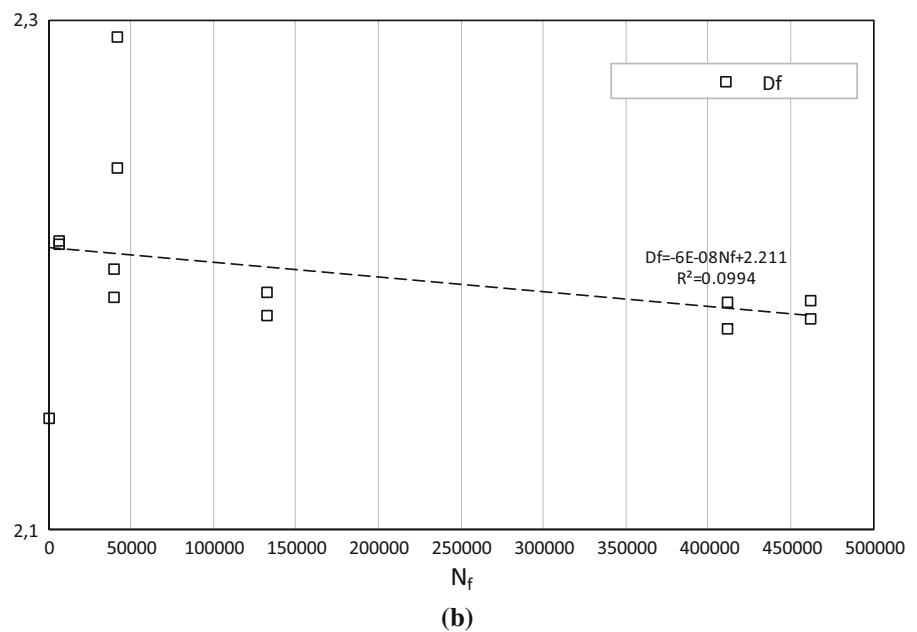
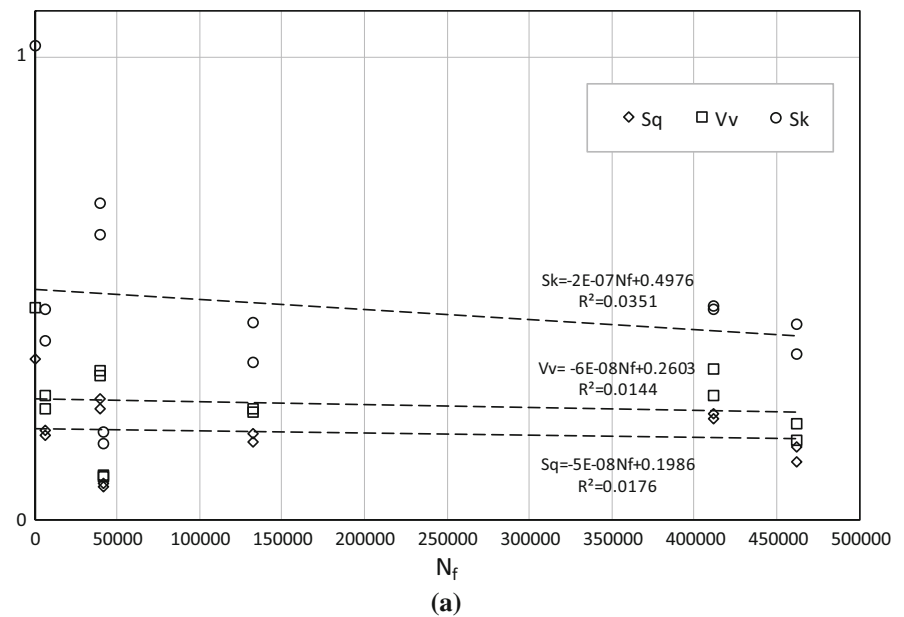
4.2 Fracture surface parameters extreme cases

4.2.1 Root average square height Sq maximum and minimum values

The Abbott–Firestone plots presented in Fig. 13 shows the distribution of heights as well as the cumulated curves for two different specimens. In general, for the Abbott–Firestone plot, the maximum values of the Sq in all cases tested demonstrate that

histogram distribution is more even. This occurs because the largest measured Sq value (specimen B3b) has the lowest depth distribution value (about 13%). On the other hand, the lowest Sq value, occurring for the C6a specimen, generates the highest percentages, amounting to approximately 15%.

Fig. 10 Fatigue life N_f vs. fracture surface parameters, for: **a** S_q , V_v , S_k ; and **b** fractal dimension D_f



4.2.2 Core roughness depth S_k distribution

For the following two sections, 4.2.2 and 4.2.3, we employed functional parameters, which fall into two categories: stratified surface and volume parameters, respectively. These parameters are derived from the Abbott-Firestone curve of the surface topography.

Core roughness depth S_k is a measure of the peak-to-valley height of the surface with predominant peaks

and valleys removed. From Figs. 9a and 14, we conclude that S_k increases with stress level. For example, an increase in the mean stress level σ_m from 54 to 180 MPa results in an increase in S_k from 0.17 to 1.02 mm (500% increase).

S_{pk} and S_{vk} are independently released by the right-angled triangle heights, which are defined on the intersections of upper material ratio S_{mk1} and lower material ratio S_{mk2} with the material ratio curves,

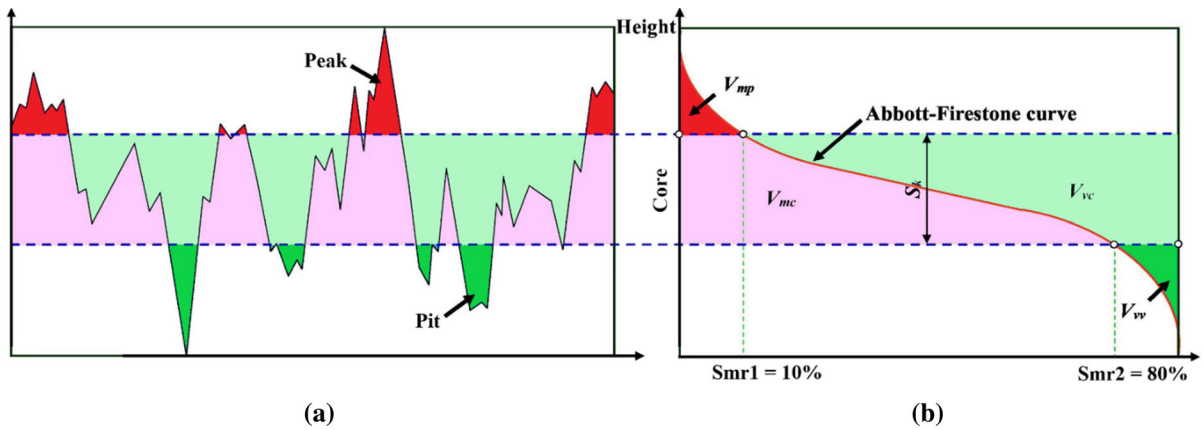


Fig. 11 Graphical presentation of the functional (volume) parameters: **a** an exemplary surface profile; **b** functional (volume) parameters of Abbott–Firestone curve according to ISO 25178. Adopted from (Macek 2021)

Fig. 12 Relationship between fractal dimension D_f , void volume V_v , core roughness depth S_k and root average square height S_q values for the SLM specimens

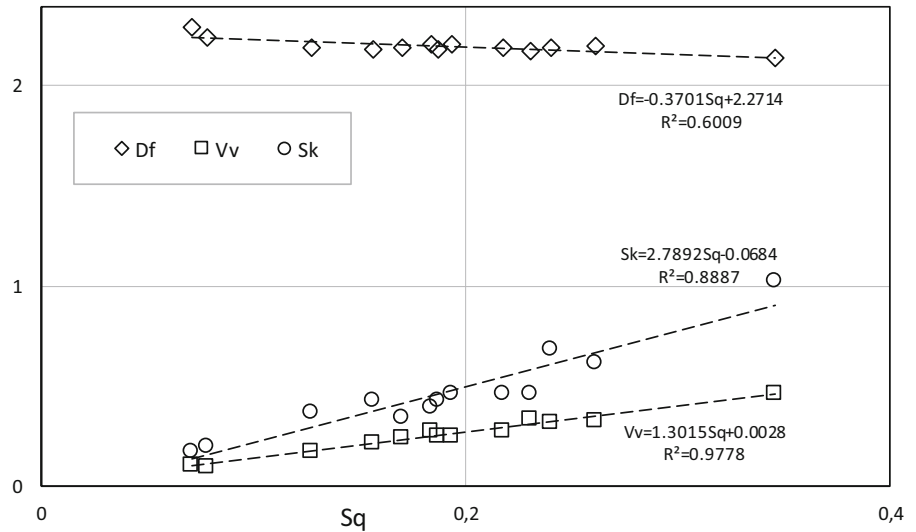
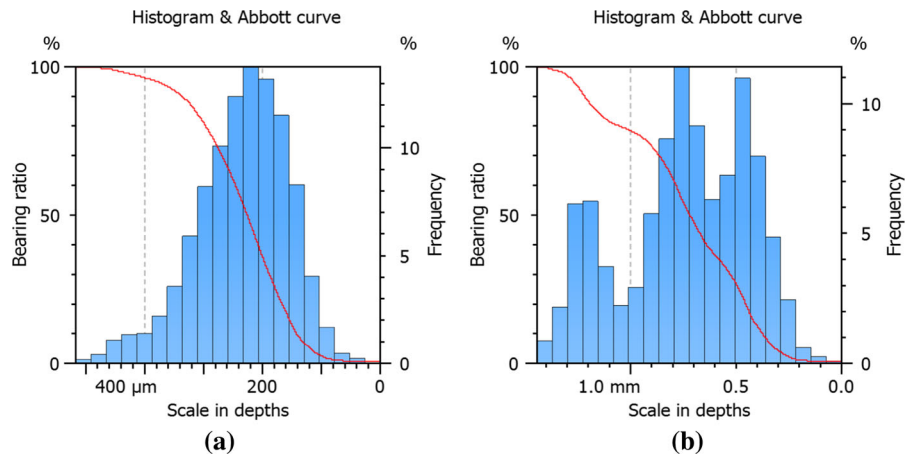
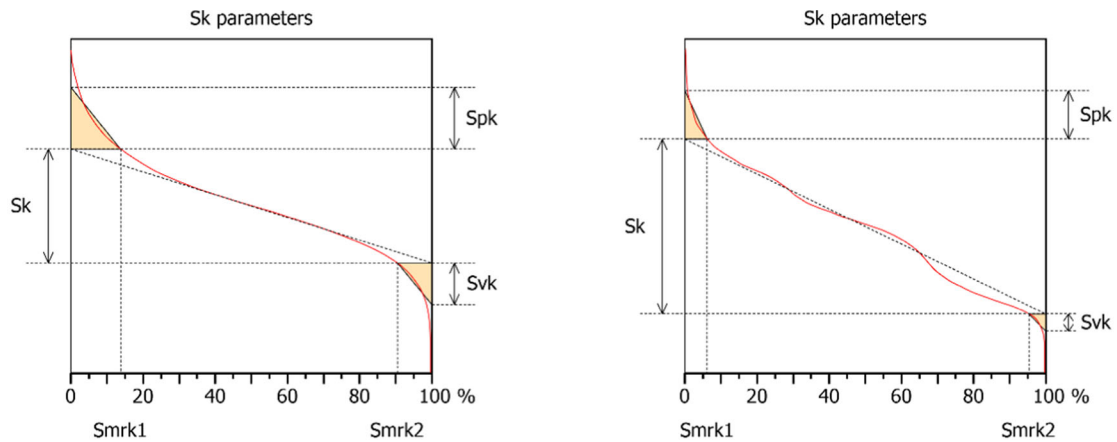


Fig. 13 The depth histograms of the fracture surfaces: **a** minimum S_q value (specimen C6a); and **b** maximum S_q value (specimen B3b). The vertical axis represents the bearing ratio [%], and the horizontal axis represents the depths (measurement unit)





Information		
Filter settings	Unfiltered.	
Parameters	Value	Unit
Sk	166.56	μm
Spk	90.56	μm
Svk	61.06	μm
Smrk1	13.75	%
Smrk2	90.47	%
Sak1	6226121.64	$\mu\text{m}^3/\text{mm}^2$
Sak2	2908389.81	$\mu\text{m}^3/\text{mm}^2$

(a)

Information		
Filter settings	Unfiltered.	
Parameters	Value	Unit
Sk	1.02	mm
Spk	0.28	mm
Svk	0.10	mm
Smrk1	6.19	%
Smrk2	95.26	%
Sak1	8.80e-03	mm^3/mm^2
Sak2	2.38e-03	mm^3/mm^2

(b)

Fig. 14 Representation of functional (stratified) parameters in Abbott-Firestone curve for the specimen: **a** C6a; and **b** B3b

respectively. Reduced peak height Spk is the height difference between the Abbott-Firestone curve and the equivalent line at 0% material ratio. Spk parameter expresses the average of peak heights above the core surface. In Fig. 14, we can see that for a specimen with a minimum Sk (specimen C6a), Spk occurs at Smrk1 = 13.75% and takes a small value (90.1 μm), with Svk = 61 μm . In addition, for the maximum Sk (specimen B3b), Spk occurs at Smrk1 = 6.19%, and Svk is relatively low (0.1 mm) with Smrk2 being over 95%.

4.2.3 Fracture surface void volume Vv relations

The functional parameters considered included Vm, Vv, Vmp, Vmc, Vvc and Vvv, for which the areal material ratio $p = 10\%$ and $q = 80\%$ were specified. A graphical interpretation of the functional parameters is presented on the Abbott-Firestone curve in Fig. 15. All of the mentioned functional parameters assume

higher values for the specimen subjected to the highest fatigue loadings.

4.2.4 Fractal dimension Df extreme values

The algorithm chosen to estimate Df is called enclosing boxes (Macek 2019b). In Fig. 16, we can see that the scale of analysis takes the largest values (> 1 mm) for the specimen with the maximum fractal dimension $Df = 2.29$ (specimen C6a).

4.3 Effect of structure and fatigue loadings on fracture morphology using SEM and Micro-CT

Comparison of fracture surfaces obtained for different fatigue testing conditions, observed using SEM is presented in Fig. 17, while the variability of porosity and pore size along the sample axis, after mechanical loading revealed using Micro-CT, is shown in Fig. 18.

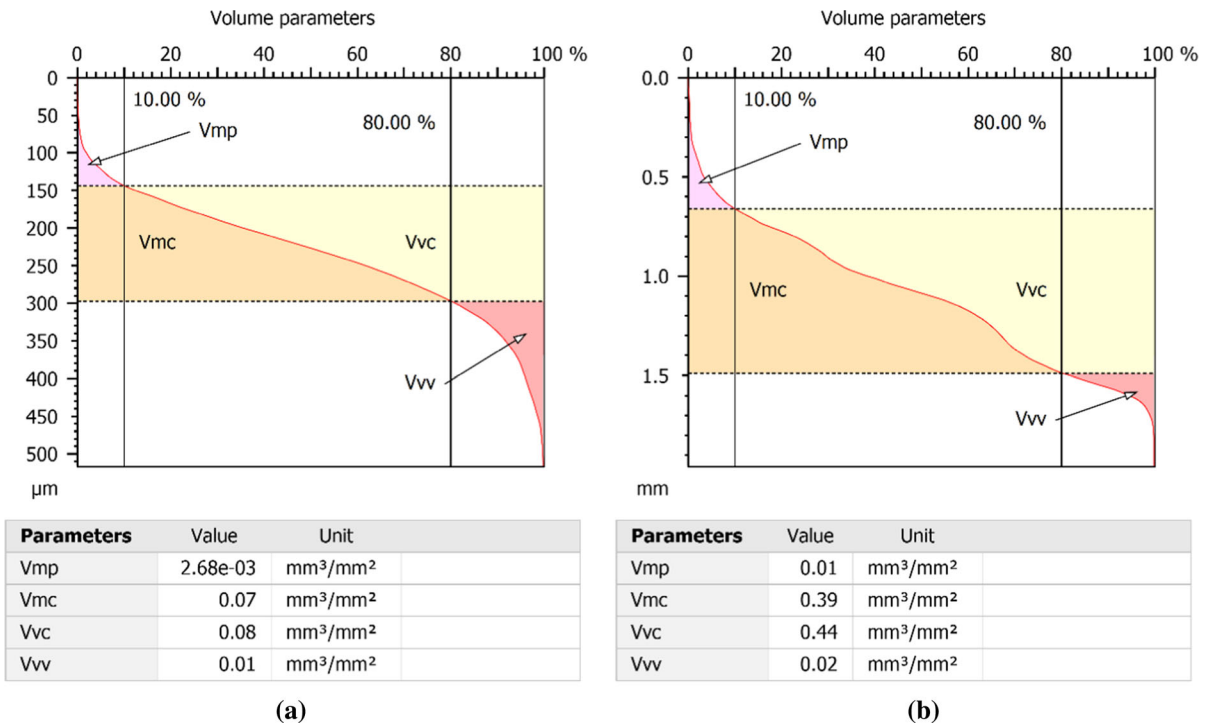


Fig. 15 Representation of functional (volume) parameters in Abbott-Firestone curve for the specimen: **a** C6b (minimum stress level); and **b** B3b (maximum stress level)

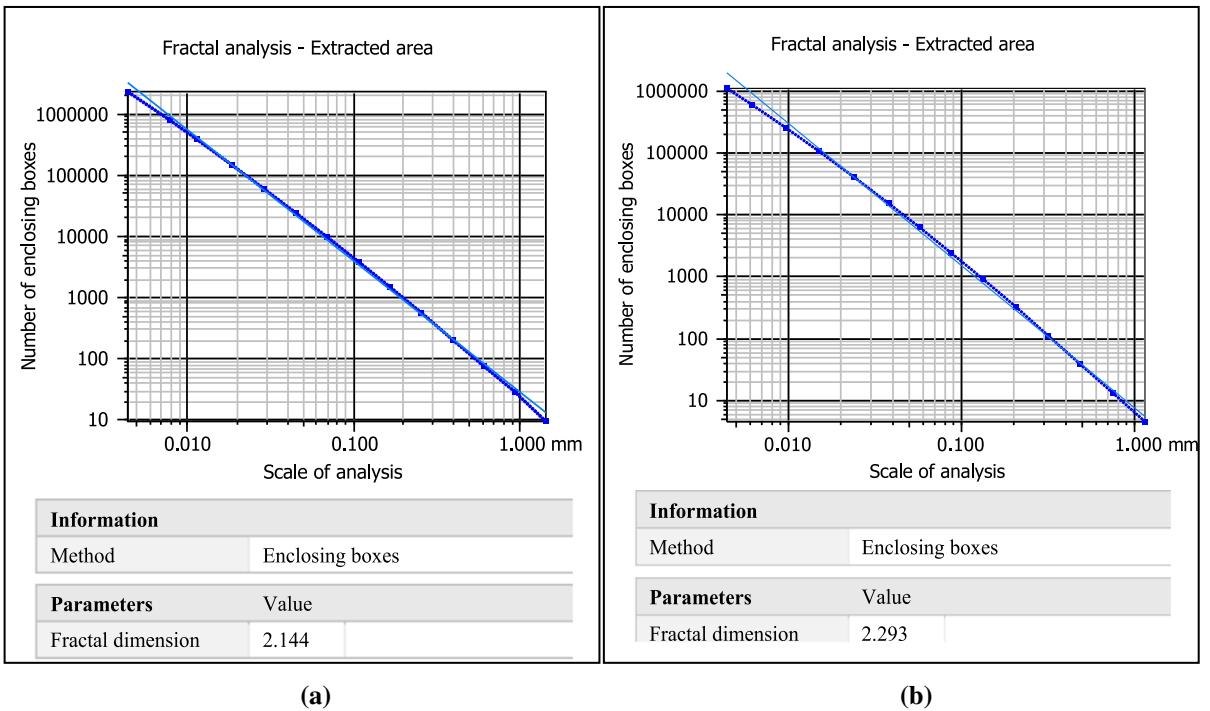
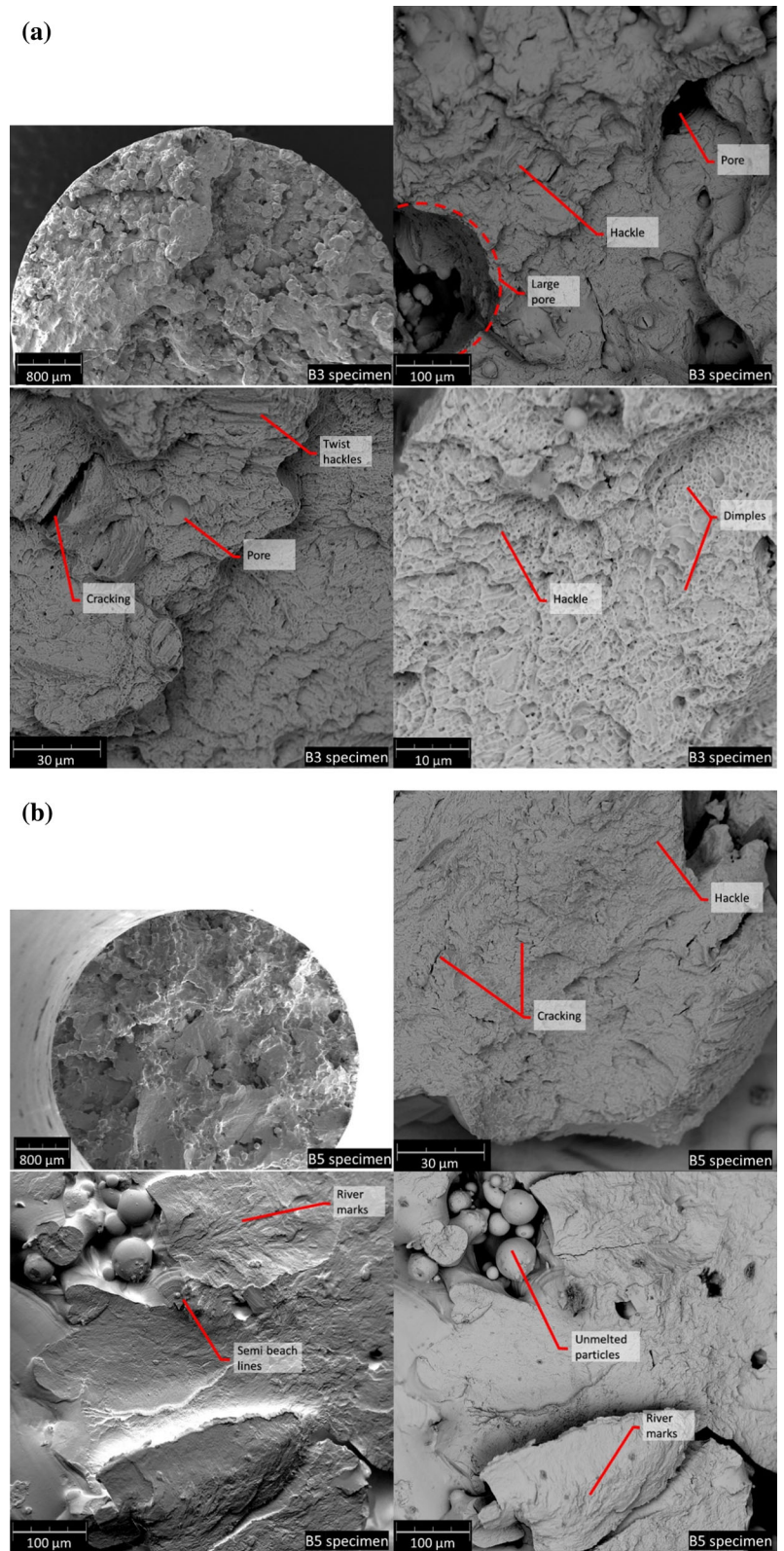


Fig. 16 The fractal dimensions D_f with slope values and coefficients of correlation R^2 determined by the enclosing boxes method for analysed cases: **a** minimum D_f value (specimen B3b); **b** maximum D_f value (specimen C6a)

Fig. 17 The fracture morphology: **a** specimen fractured at high stress level, B3; **b** fracture of low stress level, B5 (SEM, BSE and topographic modes)



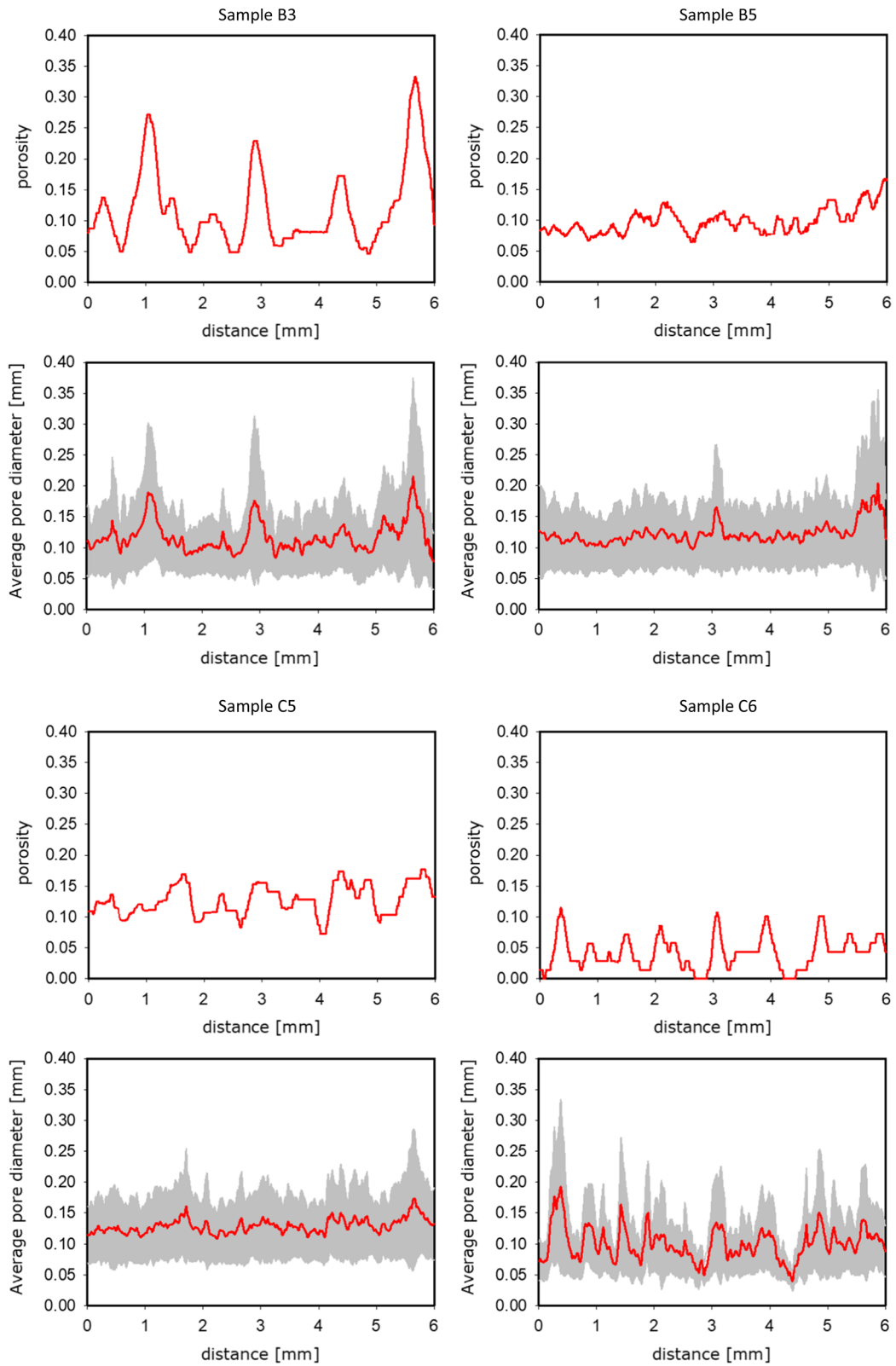


Fig. 18 The variability of porosity and pore size along the sample axis (micro-CT)

Fractographic analysis of conventionally manufactured H13 steel (specimen A15) and SLM specimens' fractures given in Fig. 6 allows to state that SLM additive manufactured samples do not exhibit classic fatigue fracture surfaces usually showing initiation, crack propagation and catastrophic rupture areas, likewise specimen A15 of Fig. 6. It derives mainly from the fact that additively manufactured metallic structure has a much more complex structure consisting of fully melted material and unmelted powder particles and pores which influences the fatigue properties and fracture structure. The effect of porosity on fatigue response is clear by comparing, for instance, both the C5 and C6 specimens, which were tested under the same stress loading conditions (see Table 2). Nevertheless, the former exhibited a fatigue life 10 times higher than the latter. A closed analysis of Fig. 18 shows that the average porosity of the C6 specimens is higher than that of the C5 specimen. However, if we compare the average pore diameters, the former has higher values and closer to the surface which eases the fatigue crack initiation process.

Another interesting outcome is that the average pore size observed by SEM in the fractured surfaces, see Fig. 17, is in the range of pore diameter estimated by Micro-CT (Fig. 18) and it varies from 0.08 to 0.15 mm. There are also oscillations that are correlated with changes in porosity, which proves that the pore distribution is heterogeneous along the sample—in areas with high porosity, the pores are larger than in areas with less porosity, see Fig. 8. In the C5 sample, the mean value of the porosity increased to the value of about 12%. Also visible are oscillations with a slightly smaller amplitude than in sample C6. On the other hand, the mean value of the pore size increased slightly; however, it shows much smaller oscillations than in the C6 sample. This proves that the average pore size along the sample axis is practically constant after a greater number of cycles. It can therefore be concluded that the greater number of cycles resulted in an increase in porosity and in the uniformity of the pore size. Interior porosity is visualised in Fig. 8 and can be read from the fracture surface observed via SEM, Fig. 17. Therefore, Fig. 17a shows coarser pores than those observed in the case of samples damaged with lower stresses, see Fig. 17b. Moreover, SEM fractographic investigations confirm that the samples tested with the high loading level, likewise B3 specimen (see Fig. 17a), present the rougher fracture

surface than those tested with lower loadings, likewise specimen B5 (see Fig. 17b). High load-tested specimens present the rough fracture surfaces in which dimples are visible. On the other hand, the higher number of cycles to failure N_f results in the presence of semi beach lines and the predominant fracture mechanism is transgranular fracture mode with the presence of cleavage fracture with river patterns. Moreover, the microstructure of SLM manufactured specimens affects crack propagation. The component porosity and unmelted powder particles act as internal notch and facilitate fatigue damage. These structural features originate from fatigue cracking and the fracture makings; likewise, hackles and cracks are visible.

Concluding, both SEM and Micro-CT results are in agreement and confirm the effect of fatigue-load conditions on the morphology of fractures.

5 Conclusions

In the present work, the fracture surface behaviour of an AISI H13 steel obtained by SLM subjected to uniaxial fatigue loading was characterised using different texture topology parameters. The objectives initially proposed were fulfilled, being possible to draw the following conclusions:

- There is a strong influence of the fatigue loading applied during the tests on the fracture surface roughness characterised via the core height, S_k , parameters;
- The fractographic evaluation conducted using scanning electron microscopy confirms the predominant fracture mechanism is transgranular fracture.
- From the quantitative analysis of the fracture surface topography, it is clear that the larger the loading applied on the specimen, the rougher the fracture surface, because the ductile fracture mode dominates.
- Fractographic investigations show that the pores and unmelted particles facilitate the fatigue fracture process. Fracture makings likewise hackles, dimples, river marks and cracks are visible on surface, irrespective of the applied stress.
- The greater number of cycles, i.e. the reduction of the applied stress level, resulted not only in an decrease in porosity after mechanical loading, but

also in the uniformity of the pore size. In addition, porosity changed along the length of the sample for the most stressed samples.

- This comprehensive quantitative and qualitative fracture analysis is beneficial to predict the failure conditions of metallic structures, especially in case of AM materials subjected to fatigue loading.

Moreover, measurements of fracture surfaces and their quantitative analysis, along with fractography, contribute to a better understanding of the fatigue failure processes.

Acknowledgements Authors acknowledge Fundação para a Ciência e a Tecnologia (FCT-MCTES) for its financial support via the project UIDB/00667/2020 (UNIDEMI) and UIDB/00285/2020 (CEMMPRE). Authors also acknowledge Science and Technology Park in Opole for enabling access to fatigue test equipment. Financial support of these studies from Gdańsk University of Technology by the DEC-10/2021/IDUB/IV.2/ EUROPIUM grant under the Europium Short-Term Outgoing visit—“Excellence Initiative—Research University” program, and also of the Lublin University of Technology-Regional Excellence Initiative, funded by the Polish Ministry of Science and Higher Education (contract no. 030/RID/2018/19) is gratefully acknowledged.

Open Access This article is licensed under a Creative Commons Attribution 4.0 International License, which permits use, sharing, adaptation, distribution and reproduction in any medium or format, as long as you give appropriate credit to the original author(s) and the source, provide a link to the Creative Commons licence, and indicate if changes were made. The images or other third party material in this article are included in the article's Creative Commons licence, unless indicated otherwise in a credit line to the material. If material is not included in the article's Creative Commons licence and your intended use is not permitted by statutory regulation or exceeds the permitted use, you will need to obtain permission directly from the copyright holder. To view a copy of this licence, visit <http://creativecommons.org/licenses/by/4.0/>.

References

- Abbott EJ, Firestone FA (1933) Specifying surface quality. *Mech Eng* 65:569–572
- Allum J, Gleadall A, Silberschmidt VV (2020) Fracture of 3D-printed polymers: crucial role of filament-scale geometric features. *Eng Fract Mech* 224:106818. <https://doi.org/10.1016/J.ENGFRACMECH.2019.106818>
- Beaman JJ, Deckard CR (1989) Selective laser sintering with assisted powder handling

- Carneiro L, Jalalahmadi B, Ashtekar A, Jiang Y (2019) Cyclic deformation and fatigue behavior of additively manufactured 17–4 PH stainless steel. *Int J Fatigue* 123:22–30. <https://doi.org/10.1016/j.ijfatigue.2019.02.006>
- Cisko A, Jordon J, Avery D, Liu T, Brewer L, Allison P et al (2019) Experiments and modeling of fatigue behavior of friction stir welded aluminum lithium alloy. *Metals* 9:293. <https://doi.org/10.3390/met9030293>
- De Jesus J, Borges M, Antunes F, Ferreira J, Reis L, Capela C (2021) A novel specimen produced by additive manufacturing for pure plane strain fatigue crack growth studies. *Metals*. <https://doi.org/10.3390/met11030433>
- Deepak Lawrence K, Shanmugamani R, Ramamoorthy B (2014) Evaluation of image based Abbott–Firestone curve parameters using machine vision for the characterization of cylinder liner surface topography. *Measurement* 55:318–334. <https://doi.org/10.1016/J.MEASUREMENT.2014.05.005>
- Feldkamp LA, Davis LC, Kress JW (1984) Practical cone-beam algorithm. *J Opt Soc Am A* 6:612–619
- Fisher K, Marquis E (2016) Comparing plasma-FIB and Ga-FIB preparation of atom probe tomography samples. *Microsc Microanal*. <https://doi.org/10.1017/S1431927616004311>
- Fonseca EB, Gabriel AHG, Araújo LC, Santos PLL, Campo KN, Lopes ESN (2020) Assessment of laser power and scan speed influence on microstructural features and consolidation of AISI H13 tool steel processed by additive manufacturing. *Addit Manuf* 34:101250. <https://doi.org/10.1016/j.addma.2020.101250>
- Garcias J, Martins R, Branco R, Marciniak Z, Macek W, Pereira C, Santos C (2021) Quasi-static and fatigue behaviour of an AISI H13 steel obtained by additive manufacturing and conventional method. *FFEMS*. <https://doi.org/10.1111/ffe.13565>
- Hebda E, Bukowczan A, Michałowski S, Wroński S, Urbaniak P, Kaczmarek M et al (2020) Examining the influence of functionalized POSS on the structure and bioactivity of flexible polyurethane foams. *Mater Sci Eng C* 108:110370. <https://doi.org/10.1016/J.MSEC.2019.110370>
- Huang H, Feng R (2006) Dynamic tribological response of SiC fracture surfaces. *Mech Mater* 38:186–202. <https://doi.org/10.1016/j.mechmat.2005.06.009>
- ISO - ISO 25178-2:2012 (2020) Geometrical product specifications (GPS)—Surface texture: Areal—Part 2: Terms, definitions and surface texture parameters. <https://www.iso.org/standard/42785.html>. Accessed 28 Dec 2020
- Kahlin M, Ansell H, Basu D, Kerwin A, Newton L, Smith B et al (2020) Improved fatigue strength of additively manufactured Ti6Al4V by surface post processing. *Int J Fatigue* 134:105497. <https://doi.org/10.1016/J.IJFATIGUE.2020.105497>
- Khosravani MR, Berto F, Ayatollahi MR, Reinicke T (2020) Fracture behavior of additively manufactured components: a review. *Theor Appl Fract Mech* 109:102763. <https://doi.org/10.1016/j.tafmec.2020.102763>
- Kida K, Ishida M, Mizobe K, Yoshida I, Tamura A, Nakane K (2017) Fatigue of low carbon alloy steel (JIS S45C) and a new method of fracture surface analysis. vol. 893 MSF. <https://doi.org/10.4028/www.scientific.net/MSF.893.181>
- Kowal M, Szala M (2020) Diagnosis of the microstructural and mechanical properties of over century-old steel railway

- bridge components. *Eng Fail Anal* 110:104447. <https://doi.org/10.1016/J.ENGFAILANAL.2020.104447>
- Kurzynowski T, Chlebus E, Kuźnicka B, Reiner J (2012) Parameters in selective laser melting for processing metallic powders. In: Beyer E, Morris T (eds) *High power laser mater. process. lasers beam deliv. diagn. Appl*, vol 8239. SPIE, Bellingham, p 823914
- Lauschmann H, Šiška F (2012) The reference texture: a proposal of a physical explanation. *Int J Fatigue* 43:120–127. <https://doi.org/10.1016/J.IJFATIGUE.2012.03.002>
- Macek W (2019a) Post-failure fracture surface analysis of notched steel specimens after bending-torsion fatigue. *Eng Fail Anal*. <https://doi.org/10.1016/j.engfailanal.2019.07.056>
- Macek W (2019b) Fractal analysis of the bending-torsion fatigue fracture of aluminium alloy. *Eng Fail Anal* 99:97–107. <https://doi.org/10.1016/j.engfailanal.2019.02.007>
- Macek W (2021) Fracture areas quantitative investigating of bending-torsion fatigued low-alloy high-strength steel. *Metals* 11:1620. <https://doi.org/10.3390/MET11101620>
- Macek W, Branco R, Trembacz J, Costa JD, Ferreira JAM, Capela C (2020a) Effect of multiaxial bending-torsion loading on fracture surface parameters in high-strength steels processed by conventional and additive manufacturing. *Eng Fail Anal*. <https://doi.org/10.1016/j.engfailanal.2020.104784>
- Macek W, Branco R, Szala M, Marciniak Z, Ulewicz R, Sczygiol N et al (2020b) Profile and areal surface parameters for fatigue fracture characterisation. *Materials* 13:3691. <https://doi.org/10.3390/ma13173691>
- Macek W, Owsiński R, Trembacz J, Branco R (2020c) Three-dimensional fractographic analysis of total fracture areas in 6082 aluminium alloy specimens under fatigue bending with controlled damage degree. *Mech Mater*. <https://doi.org/10.1016/j.mechmat.2020.103410>
- Macek W, Rozumek D, Królczyk GM (2020d) Surface topography analysis based on fatigue fractures obtained with bending of the 2017A–T4 alloy. *Meas J Int Meas Confed*. <https://doi.org/10.1016/j.measurement.2019.107347>
- Macek W, Marciniak Z, Branco R, Rozumek D, Królczyk GM (2021a) A fractographic study exploring the fracture surface topography of S355J2 steel after pseudo-random bending-torsion fatigue tests. *Measurement* 178:109443. <https://doi.org/10.1016/j.measurement.2021.109443>
- Macek W, Branco R, Korpyś M, Łagoda T (2021b) Fractal dimension for bending–torsion fatigue fracture characterisation. *Measurement*. <https://doi.org/10.1016/J.MEASUREMENT.2021.109910>
- Moussa A, Melancon D, El Elmi A, Pasini D (2021) Topology optimization of imperfect lattice materials built with process-induced defects via powder bed fusion. *Addit Manuf* 37:101608. <https://doi.org/10.1016/j.addma.2020.101608>
- Nagahama T, Mizoguchi T, Yonehara M, Kyogoku H (2019) The porosity and mechanical properties of h13 tool steel processed by high-speed selective laser melting
- Pomberger S, Stoschka M, Aigner R, Leitner M, Ehart R (2020) Areal fatigue strength assessment of cast aluminium surface layers. *Int J Fatigue* 133:105423. <https://doi.org/10.1016/J.IJFATIGUE.2019.105423>
- Razavi SMJ, Berto F (2018) Fatigue strength of notched specimens made of Ti-6Al-4V produced by Selected Laser Melting technique. *Procedia Struct Integr* 13:74–8. <https://doi.org/10.1016/j.prostr.2018.12.013>
- Romano S, Nezhadfar PD, Shamsaei N, Seifi M, Beretta S (2020) High cycle fatigue behavior and life prediction for additively manufactured 17–4 PH stainless steel: effect of sub-surface porosity and surface roughness. *Theor Appl Fract Mech* 106:102477. <https://doi.org/10.1016/J.TAFMEC.2020.102477>
- Sampath D, Akid R, Morana R (2018) Estimation of crack initiation stress and local fracture toughness of Ni-alloys 945X (UNS N09946) and 718 (UNS N07718) under hydrogen environment via fracture surface topography analysis. *Eng Fract Mech* 191:324–343. <https://doi.org/10.1016/j.engfracmech.2017.12.010>
- Santos LMS, Ferreira JAM, Jesus JS, Costa JM, Capela C (2016) Fatigue behaviour of selective laser melting steel components. *Theor Appl Fract Mech* 85:9–15. <https://doi.org/10.1016/j.tafmec.2016.08.011>
- Slámečka K, Pokluda J, Kianicová M, Major S, Dvořák I (2010) Quantitative fractography of fish-eye crack formation under bending-torsion fatigue. *Int J Fatigue*. <https://doi.org/10.1016/j.ijfatigue.2009.07.009>
- Țălu Ș, Matos RS, Pinto EP, Rezaee S, Mardani M (2020) Stereometric and fractal analysis of sputtered Ag–Cu thin films. *Surf Interfaces* 21:100650. <https://doi.org/10.1016/j.surf.2020.100650>
- Todhunter LD, Leach RK, Lawes SDA, Blateyron F (2017) Industrial survey of ISO surface texture parameters. *CIRP J Manuf Sci Technol* 19:84–92. <https://doi.org/10.1016/J.CIRPJ.2017.06.001>
- Volume Graphics GmbH, editor. Reference Manual VGStudio Max Release 2.0; <http://www.volumegraphics.com/en/products/vgstudio-max/>. Accessed 8 Oct 2013
- Walczak M, Szala M (2021) Effect of shot peening on the surface properties, corrosion and wear performance of 17–4PH steel produced by DMLS additive manufacturing. *Archiv Civ Mech Eng* 21:157. <https://doi.org/10.1007/s43452-021-00306-3>
- Wang Z, Wu W, Qian G, Sun L, Li X, Correia JAFO (2019) In-situ SEM investigation on fatigue behaviors of additive manufactured Al–Si10–Mg alloy at elevated temperature. *Eng Fract Mech* 214:149–163. <https://doi.org/10.1016/J.ENGFRACTMECH.2019.03.040>
- Weng F, Liu Y, Chew Y, Yao X, Sui S, Tan C et al (2020) IN100 Ni-based superalloy fabricated by micro-laser aided additive manufacturing: correlation of the microstructure and fracture mechanism. *Mater Sci Eng A* 788:139467. <https://doi.org/10.1016/j.msea.2020.139467>
- Xue L, Chen J, Wang SH (2013) Freeform laser consolidated H13 and CPM 9V tool steels. *Metallogr Microstruct Anal* 2:67–78. <https://doi.org/10.1007/s13632-013-0061-0>
- Żebrowski R, Walczak M, Korga A, Iwan M, Szala M (2019) Effect of shot peening on the mechanical properties and cytotoxicity behaviour of titanium implants produced by 3D printing technology. *J Healthc Eng*. <https://doi.org/10.1155/2019/8169538>

Publisher's Note Springer Nature remains neutral with regard to jurisdictional claims in published maps and institutional affiliations.